PAPER • OPEN ACCESS

Impurity transport study based on measurement of visible wavelength high-n charge exchange transitions at W7-X

To cite this article: Colin Swee *et al* 2024 *Nucl. Fusion* **64** 086062

View the article online for updates and enhancements.

Impurity transport study based on measurement of visible wavelength high-n charge exchange transitions at W7-X

Colin Swee[1,*] , **Benedikt Geiger**[1] , **Oliver Ford**[2], **Mark Nornberg**[1] , **Martin O'Mullane**[3] , **Peter Poloskei**[2] , **Felix Reimold**[2], **Thilo Romba**[2] , **Thomas Wegner**[2] **and the W7-X Team**[a]

[1] Department of Nuclear Engineering and Engineering Physics, University of Wisconsin-Madison, Madison, WI 53706, United States of America
[2] Max-Planck Institute for Plasma Physics, 17491 Greifswald, Germany
[3] University of Strathclyde, 107 Rottenrow, Glasgow G4 0N, United Kingdom of Great Britain and Northern Ireland

E-mail: ckswee@wisc.edu

Abstract
A recently installed high-speed charge exchange diagnostic at the W7-X stellarator has been used to identify several high-n Rydberg emission lines near 500 nm following impurity injections. The wavelengths of observed high-n Rydberg transitions are independent of the impurity species and originate from ions with ionization states ranging from 14+ to 45+ suggesting that this approach can be applied to a variety of heavy impurities. Moreover, little to no passive signal is observed since the high-n energy levels are unlikely to be populated by electron impact excitation. The combination of the newly developed diagnostic and the observation of high-n Rydberg states provides spatially resolved, high-speed measurements of multiple charge states which are analyzed in a Bayesian inference framework to determine both impurity diffusion and convection profiles. Measurements from the 2023 experimental campaign conclusively show high diffusion and an inward pinch in the core, well above predictions by neoclassical theory.

(Some figures may appear in colour only in the online journal)

---

[a] See Grulke *et al* 2024 (https://doi.org/10.1088/1741-4326/ad2f4d) for the W7-X Team.
[*] Author to whom any correspondence should be addressed.

1. Introduction

To reliably operate future fusion power plants, a detailed understanding of the transport of heavy impurities must be achieved [1, 2]. Heavy impurities can originate from plasma-facing components or deliberate injections designed to control divertor heat fluxes. These impurities maintain bound electrons even at fusion-relevant temperatures leading to intense line radiation and corresponding radiative cooling in the plasma core, which will reduce the fusion energy gain or even terminate plasmas early. Specifically for the case of stellarator plasmas, electrons and ions can experience unbalanced fluxes due to their differing collisionality. To maintain ambipolarity, an inward radial electric field typically develops which affects the impurities through an inward pinch velocity. Such observations have been made in several stellarator experiments [3–7]. This is in contrast to the tokamak where the ambipolarity condition is intrinsic to the axisymmetry [8]. Additionally, previous modeling work has shown that contributions from turbulence can contribute significantly to the convection velocity [9, 10]. Therefore, to fully understand the balance between turbulent and neoclassical contributions, the experimental characterization of impurity convection velocities in stellarators is of great importance for the design of future reactors.

For the study of highly charged impurities in fusion plasmas, impurity injections using laser blow-off (LBO) [11–20] are routinely performed and the subsequent evolution of line emissions is monitored by means of vacuum ultraviolet (VUV) spectroscopy [21–25]. This emission can be observed at high time resolutions of >1 kHz since radiation is strong in the wavelength range between 1 and 100 nm. While certain VUV/EUV diagnostics have been designed to provide spatially resolved impurity density measurements [26, 27], those present on W7-X measure line-integrated signals and therefore lack information on the localization of impurity emission. In the context of impurity transport studies, the consequence of utilizing line-integrated signals can manifest as weak constraints on the convection velocity [21].

As either an alternative or a complement to VUV spectroscopy, charge exchange recombination spectroscopy (CXRS) is available. CXRS measures well-localized emission following charge exchange (CX) between the neutral beam and impurity ions. This good spatial resolution is due to prompt emission following CX reactions since CX preferentially leaves electrons in excited states with principle quantum numbers following the rough scaling of $n \approx (q+1)^{3/4}$ where q is the net charge of the ion [28, 29]. Note that energy levels higher and lower than this prediction can be populated with cross-sections depending on the neutral kinetic energy [28].

Typically, CXRS measurements are utilized to determine ion temperatures and rotation profiles of low-Z impurity ions which are assumed to share similar parameters with the main plasma ions. In addition, steady-state impurity density profiles for low to medium Z species are being investigated, as has been done recently at W7-X [30–32] and in the past at other devices [33–35]. However, medium to high-Z impurity

transport studies based on the combination of LBO and CXRS are not routinely performed. Two examples can be found for TFTR and the DIII-D tokamak [36, 37], but there have been no such studies performed in the stellarator literature. This can be explained in part due to the lack of high-speed CX measurements, as well as a lack of knowledge of emission lines available for heavy impurities. On devices with small background-neutral populations inside the confined region CX radiation from heavy impurities have excellent spatial resolution. Here we present the results of a new CX diagnostic at W7-X that allow for the identification of impurity emission lines from various charge states in the visible spectrum following LBO. These measurements are then used in a Bayesian framework to infer impurity transport which is, in the analyzed experimental program, anomalously large with an inward pinch in the core. The remainder of this paper is structured as follows: section 2 will discuss the experimental setup including the newly developed CXRS system installed for the OP 2.1 campaign as well as the details on modeling the impurity transport and radiation. Next, section 3 discusses the identification of several high-n Rydberg lines of interest and their inclusion in a Bayesian inference framework based on the pySTRAHL code. Finally, sections 4 and 5 provide a discussion of the experimental observations and a conclusion.

2. Methods

2.1. Experimental setup

For the OP2.1 experimental campaign at W7-X, a new CX diagnostic has been installed that views neutral beam source 7 from the AEM port (see figure 1 in [30] for a description of the beam geometry). Nine new 600 μm diameter optical fibers are used along with one additional preexisting 400 μm fiber which views near the mid-radius on the inboard side (labeled LOS #10 in figure 1). The approximate locations where the lines of sight intersect NBI 7 are shown projected on a poloidal cross-section of the W7-X magnetic field in figure 1(*a*). Here the beam density is simulated using the Monte-Carlo code pyFIDASIM [38]. In this simulation, the total hydrogen beam density is a sum of the contributions from the full, half, and third beam components which originate from the acceleration of H_1^+, H_2^+, and H_3^+, respectively, as well as neutrals in the vicinity of the beam which have become thermalized with respect to the background plasma (known as the 'halo' component). Additionally, considered in the pyFIDASIM calculation is the ground state, $n = 1$, up to the $n = 6$ excited state. Kinetic profiles used in the calculation are given in figure 10. The beam attenuation along the direction of the major radius for each energy component and the first two energy levels is given in figure 1. To determine the spatial resolution of the diagnostic, beam neutrals predicted by pyFIDASIM along a given line of sight are binned according to their respective location on the 1D radial grid and then the curve is normalized such that it integrates to 1. These so-called localization functions,
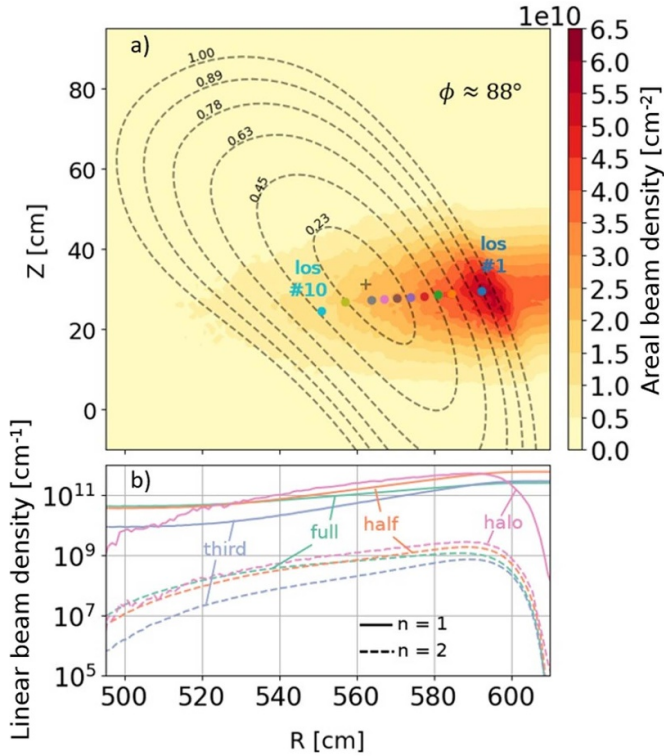
Figure 1. (*a*) Approximate locations of intersection between ten of the new CXRS diagnostic lines of sight and the 50 keV neutral beam. Shown in color-scale is the beam density integrated over the toroidal direction. (*b*) Attenuation of the various beam components for energy levels $n = 1$ and $n = 2$. Plotted densities are integrated over both the toroidal and Z directions.
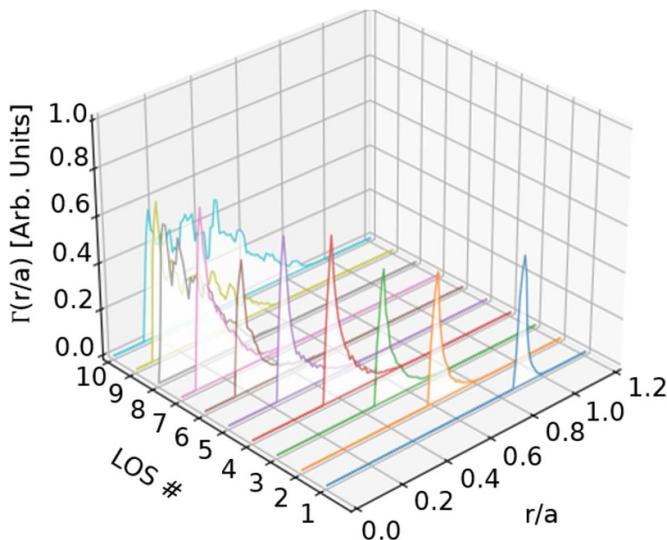

Figure 2. Radial resolution functions calculated from pyFIDASIM. Each function is normalized such that it integrates to 1. Note that lines of sight 8–10 exhibit lesser spatial localization as they are more oblique to the beam axis.

$\Gamma(r/a)$, are shown in figure 2 and indicate good spatial resolution for the outer lines of sight while there is a notable degradation in the radial localization for the most inboard three lines of sight.

To view CX emission along the W7-X neutral beams, five dual-channel spectrometers have been installed and are described in detail in a recent publication [39]. The spectrometers have been designed to maximize light throughput enabling high frame rate operation. The main design choices that provide improvements to light throughput when compared to the existing CXRS capabilities at W7-X are that of the larger diameter optical fibers as well as round to linear fiber arrangements at the spectrometer entrance that eliminate losses due to masking with an entrance slit.

The geometry of the spectrometers has been designed such that two fiber bundles can stack vertically allowing for dual channel readout of ten lines of sight. By using two channels per spectrometer, the Gaussian instrument function width (i.e. the minimum observable line width) for individual channels can be slightly broadened due to the imaged fiber bundles appearing tilted on the CCD chip. This is an imaging effect due to the vertical angle of the light incident on the spectrometer gratings (also known as the parabola effect) and can be partially corrected by rotating the fiber bundles by a few degrees leading to a slight horizontal offset between the two channels. Despite this feature, the Gaussian instrumental function widths on each channel are between 0.06 nm and 0.13 nm (see figure 3) which is sufficient to resolve all peaks of interest in this work. Andor EMCCD cameras are used as detectors for the spectrometers and operate in a frame-transfer mode where three regions of interest (ROI) are defined and their collected light vertically binned. Two of these ROIs are used for imaging the two stacked fiber bundles while the third (middle) ROI is used for CCD smearing effect detection and correction.

Finally, an absolute spectral radiance calibration has been performed for the new CXRS system via the use of an in-vessel calibration sphere. This allows for the comparison of spectral radiance, and therefore localized impurity densities between CXRS channels. However, due to a lack of effective emission data (i.e. ADAS ADF 12 coefficients) for the transitions of interest in this work, only relative intensities are compared between channels.

2.2. Forward modeling of relative intensity calibrated CX emission

Forward modeling based on the pySTRAHL code [40] is used to simulate signals from the new CX system. To translate simulated impurity density profiles at each time step into synthetic diagnostics suitable for comparison with CXRS measurements, one can pair the pySTRAHL simulated impurity densities with a model of the neutral beam calculated by the pyFIDASIM code. pySTRAHL solves the impurity transport equation for each charge state of a given impurity:

$$\frac{\partial n_z}{\partial t} = \frac{1}{r}\frac{\mathrm{d}}{\mathrm{d}r}r\left(D(r)\frac{\mathrm{d}n_z}{\mathrm{d}r} - v(r)n_z\right) - n_z\omega_\parallel + R_z + Q_z. \quad (1)$$

Here, $\omega_\parallel$ is the parallel loss rate to the divertor which is zero inside the LCFS, R_z represents sources and sinks due to ionization and recombination, and Q_z represents sourcing due to the initial ionization of the neutral charge state. For the modeling results given in section 3, the ionization, recombination,
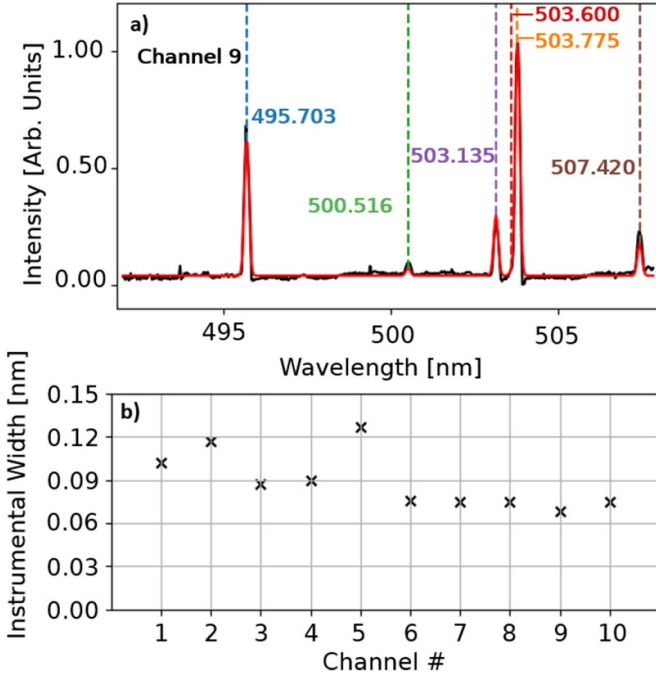
Figure 3. (*a*) Recorded (black) and fitted (red) spectra from a neon calibration lamp for one representative spectrometer channel. (*b*) The width of the fitted Gaussian instrument function for each spectrometer channel.

and CX rates necessary for use in equation (1) are the ADAS files: *'scd89_fe.dat'*, *'acd89_fe.dat'*, and *'ccd89_fe.dat'*.

To effectively utilize the CXRS method, one must first ensure that the plasma conditions allow for sufficient penetration of the beam to the core to allow for sufficiently high CX signal intensities. A simple order of magnitude calculation of the beam mean free path has been developed by Janev *et al* [41] which can be compared to the machine's minor radius of ∼50 cm. From equation (23) in [41] one calculates a beam mean free path of >20 cm for electron densities higher than 10^{20} m^{-3} and a temperature of 2 keV. This indicates that for densities of 10^{20} m^{-3}, one would expect beam attenuation to be significant.

To provide a more detailed calculation of the beam attenuation suitable for use in comparison to measured intensities, the Monte–Carlo neutral simulation code pyFIDASIM can be utilized. Given an initial trajectory and energy fraction, the code uses tabulated ionization, recombination, CX, excitation, and de-excitation rates to determine the steady-state population n-levels 1–6 for the full, half, third, and thermal energy components. Typically, only n-levels 1 and 2 contribute significantly to the CX signal [42] therefore, only those beam components are considered for modeling CX signals here. The calculated beam attenuation for the four energy components and the first two excitation levels is given in figure 1.

The local emission from a particular point in the plasma is:

$$\epsilon_{Z,\text{los}} = n_z \sum_k \left(n_{0,k,\text{full}} \alpha_{z,k,\text{full}} + n_{0,k,\text{half}} \alpha_{z,k,\text{half}} \right.$$
$$\left. + n_{0,k,\text{third}} \alpha_{z,k,\text{third}} + n_{0,k,\text{halo}} \alpha_{z,k,\text{halo}} \right). \quad (2)$$

Here, n_Z is the impurity density for charge state Z, $n_{0,k,\text{full}}$, $n_{0,k,\text{half}} \ldots$ etc are the neutral densities for the full, half, third, and halo beam components at excited state k, and $\alpha_{z,k,\text{full}}, \alpha_{z,k,\text{half}} \ldots$ etc are the effective emission coefficients for the transition of interest following CX with the various beam components. Again, note that only contributions from the first two excited states are considered when modeling the charge exchange intensity.

At the time of this publication, effective emission coefficients are not available for the high-n transitions studied here. Despite this, one can note that since charge exchange with beam neutrals is a resonant process, these effective emission coefficients depend only on the beam neutral energy which is constant along the beam path. Additionally, previous work has shown that at relevant thermal temperatures, carbon effective emission coefficient from halo neutrals has a fairly weak dependence on the ion temperature [42]. Here we make the assumption that this trend holds for iron transitions as well. Considering the assumption of constant effective emission coefficients, one can rewrite equation (2) in terms of an 'effective' beam attenuation, X_{eff}:

$$\epsilon_{Z,\text{los}} = n_z n_{0,\text{edge}} X_{\text{eff}} \propto n_z X_{\text{eff}}. \quad (3)$$

Here, $n_{0,\text{edge}}$ represents the beam neutral density at the edge before it is attenuated by the plasma. In this case, the uncertainty in X_{eff} is determined by which beam component dominates in equation (2). The densities for each beam component shown in figure 1 can be normalized and evaluated at the intersection point between the beam and each line of sight. These relative attenuation values are shown in figure 4 for each beam component and excitation level. Note that the above-defined 'effective' beam attenuation curve, X_{eff} will be bound within these values (the gray-shaded region in figure 4). The uncertainty in X_{eff} is then well defined and can be propagated into fit uncertainties when considering the Bayesian inference framework.

Forward-modeled impurity emissions from CX are then calculated by considering the radial localization and the effective beam attenuation for a given line of sight:

$$I_{\text{los}} \propto X_{\text{eff,los}} \int n_z \Gamma_{\text{los}} \mathrm{d}\rho \quad (4)$$

Here, I_{los} represents the line-integrated intensity seen by a line of sight, $X_{\text{eff,los}}$ represents the effective beam attenuation at the location where the line of sight intersects the neutral beam, n_z represents the impurity density for the charge state of interest, and Γ_{los} represents the radial localization as depicted in figure 2.
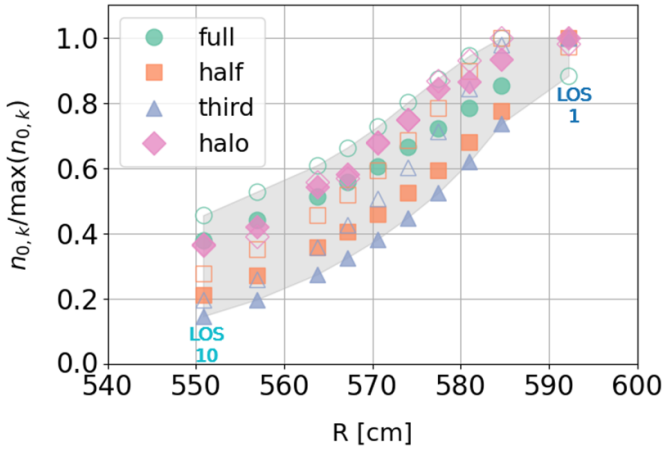
Figure 4. Simulated beam attenuation from neutral beam source 7 for program 20230314.26. Normalized beam neutral densities for each energy component and the first two excitation levels are plotted along the major radial coordinate. The markers indicate the line-integrated neutral density seen by each line of sight with filled markers representing the $n = 1$ energy level and hollow markers corresponding to $n = 2$ energy levels. The shaded region represents the domain which X_{eff} can occupy.

3. Results

3.1. Observation of impurity emission from high-n Rydberg states

During the OP 2.1 operational campaign at W7-X, the new CXRS system was set to observe spectra from the wavelength range of $\sim$495–510 nm. Data from two experimental programs are shown which used injections of either iron (20230314.26) and tungsten (20230315.30). During the impurity injections, the measured core densities are $\sim$6 × 10^{19} m^{-3} and $\sim$4 × 10^{19} m^{-3}, respectively, for programs 20230314.26 and 20230315.30. The measured core electron temperatures during the impurity injections for the two programs are $\sim$2.1 keV and $\sim$4 keV and core ion temperatures are $\sim$1.3 keV and $\sim$1.5 keV respectively.

Clear line emissions have been observed shortly after the impurity injections and have been identified as Rydberg transitions from charge exchange of impurities into high-n levels. The observation of these lines from both Fe and W illustrates that such measurements are robust to the specific impurity species. Figures 5 and 6, respectively, show recorded spectra following both an injection of Fe via the LBO method and W via encapsulated solid pellet (TESPEL) injection [43]. While the iron injection experiment is done with continuous NBI operation, the tungsten is injected into a plasma with short 30 ms 'blips'. In these experiments, three emission lines can be observed as originating from iron injection while four can be seen following the tungsten injection. These line transitions are due to charge exchange with either the neutral beam or (in the case of passive signals) charge exchange with edge neutrals.
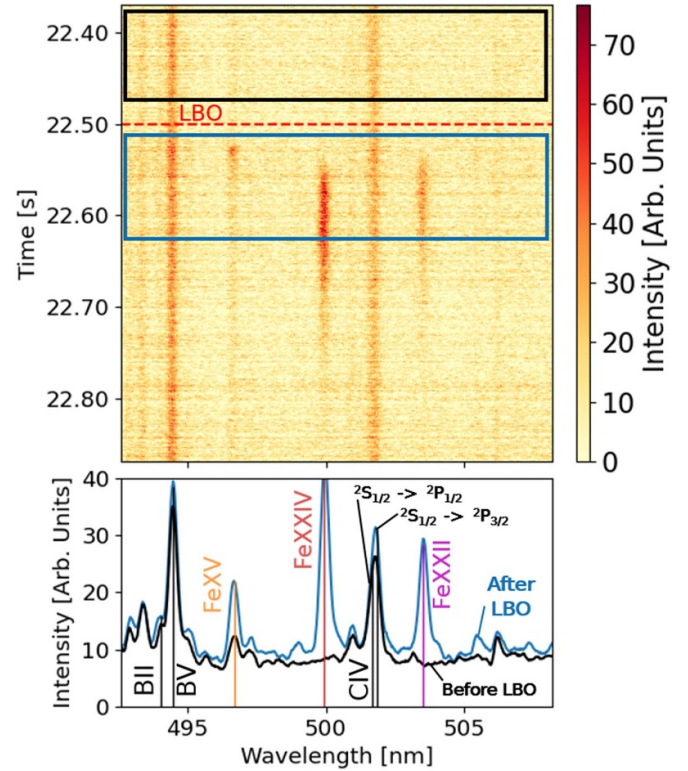

Figure 5. Spectrum following laser blow-off (LBO) injection of Fe into plasma with continuous NBI (Program # 20230314.26). The top plot shows signal intensity vs time and wavelength. Impurity emission prior-to (after) the LBO injection is time-averaged over the range specified by the black (blue) box and shown in the bottom window. The Fe XV overlaps with an Ar XV line explaining the emission before the LBO.

Typically, when calculating energy levels of heavy atoms, it is necessary to consider the quantum defect that arises due to imperfect charge screening from the inner shell electrons. However, for transitions between sufficiently high principle quantum numbers (n_1,n_2), the quantum defect can be ignored when calculating energy level differences. This allows one to accurately predict transition wavelengths using the relativistically corrected Rydberg formula [44–46]:

$$\frac{1}{n_{\text{air}}\lambda_{\text{air}}} = \frac{m_e c}{h}\left(\frac{1}{\sqrt{1 - (q+1)^2\,\alpha^2/n_2^2}} - \frac{1}{\sqrt{1 - (q+1)^2\,\alpha^2/n_1^2}}\right). \tag{5}$$

Here, n_1 and n_2 are the two energy levels for the transition, q is the charge of the ion, n_{air} is the index of refraction in air, λ_{air} is the transition wavelength in air, and α is the fine structure constant. The three emission lines following LBO injection of Fe can then be identified as originating from the Fe^{14+}, Fe^{21+}, and Fe^{23+} charge states while the four W lines originate from W^{23+}, W^{25+}, W^{45+}, and W^{47+}. Table 1 shows the calculated wavelengths for these transitions as well as several other possible transitions one may observe in this wavelength range
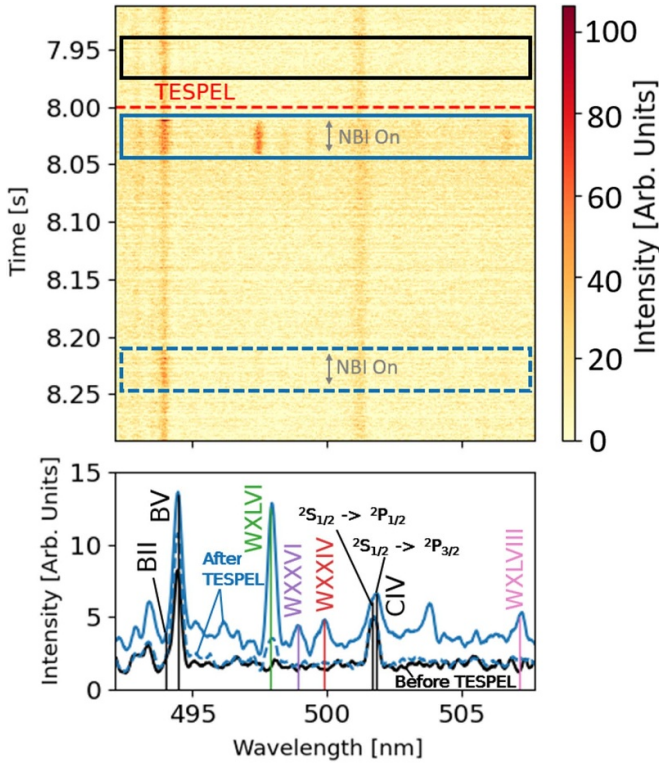
Figure 6. Figure analogous to figure 5 for pellet injection of W into plasma with pulsed beam blips (Program # 20230315.30). The time-averaged spectrum during the second beam blip 200 ms later is shown in dashed blue.

Table 1. Line transitions with calculated wavelengths in the range of 492–508 nm. Wavelengths are calculated with equation (5).

q	n_1	n_2	Predicted Wavelength (nm)
14	13	14	496.683
21	17	18	503.501
23	18	19	499.914
25	19	20	498.908
27	20	21	499.873
29	21	22	502.379
31	22	23	506.109
38	25	26	496.103
40	26	27	503.818
45	28	29	497.917
47	29	30	507.152

Figure 7. Coronal equilibrium charge state distributions for Fe (*a*) and W (*b*) as a function of temperature at an electron density of 5×10^{19} m^{-3}. For easier interpretation, only charge states which charge exchange into those given in table 1 are depicted. The specific ADF files utilized for this calculation are *'acd89_fe.dat'*, *'scd89_fe.dat'*, *'acd01_w.dat'*, and *'scd01_w.dat'*.

for other impurities. In this table, to limit the calculation to realistically observable emissions, the predicted transitions are limited to high charge state ($q > 10$), electric dipole ($\Delta n = 1$) transitions with upper energy levels, $n_2 < q$.

It is important to note that several W-emission lines are present even in the absence of the neutral beam. This can be explained via the coronal equilibrium model. For a given electron density, one can calculate the steady-state impurity charge state distributions in the absence of transport and considering the limit where recombination processes are dominated by electron capture reactions. While experimental plasmas will certainly differ from the coronal prediction due to transport,
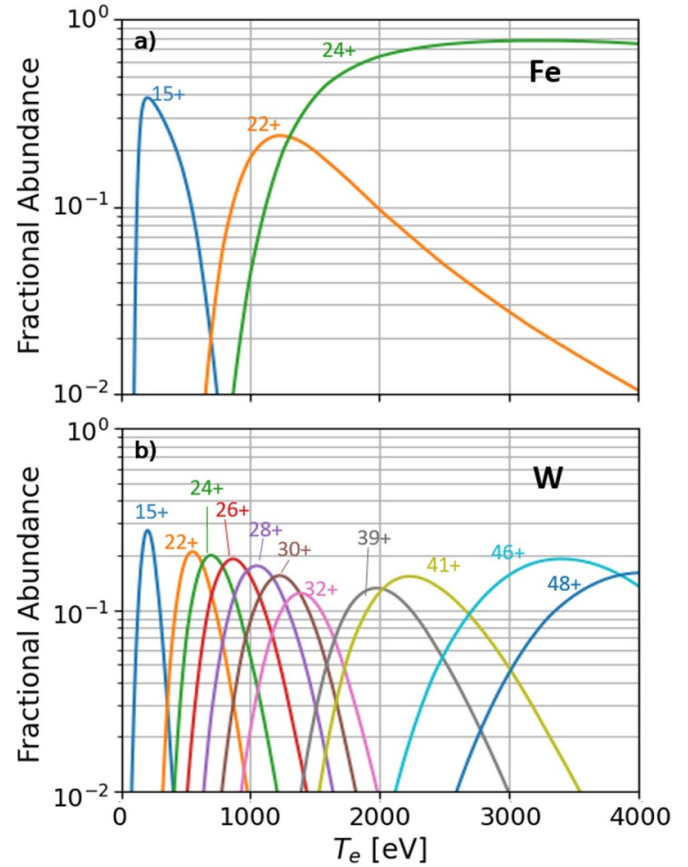
consideration of this simplified model can be useful to get a rough idea of the charge state distribution in a given temperature region. The necessary ionization and recombination rates for this calculation are tabulated and available through the Open ADAS database [47, 48].

As can be seen in figure 7, similar charge states (e.g. Fe^{23+} and W^{23+}) dominate at very different temperature ranges. While Fe^{23+} may only be present in the core, W^{23+} would likely be present closer to the plasma edge where background neutrals are present which can lead to charge exchange and therefore passive radiation. The same is true for Fe^{14+} and is additionally illustrated in figure 8 which depicts data collected from LOS # 5 during program # 20230314.41 following an iron LBO without NBI. Passive radiation from Fe^{14+} is visible after the LBO and originates near the edge. Note here that the time dynamics of the Fe XV line is complicated by the presence of puffed argon and therefore Ar XV emission.

In contrast, since electron impact excitation is unlikely to populate the energy levels considered here, passive radiation is not seen for emission from higher charge states such as Fe^{23+}. This feature can be seen in figure 9. In this experiment, LBO is injected into a plasma that has NBI blips fired at 10 Hz. The LBO is synchronized such that injection occurs during one of
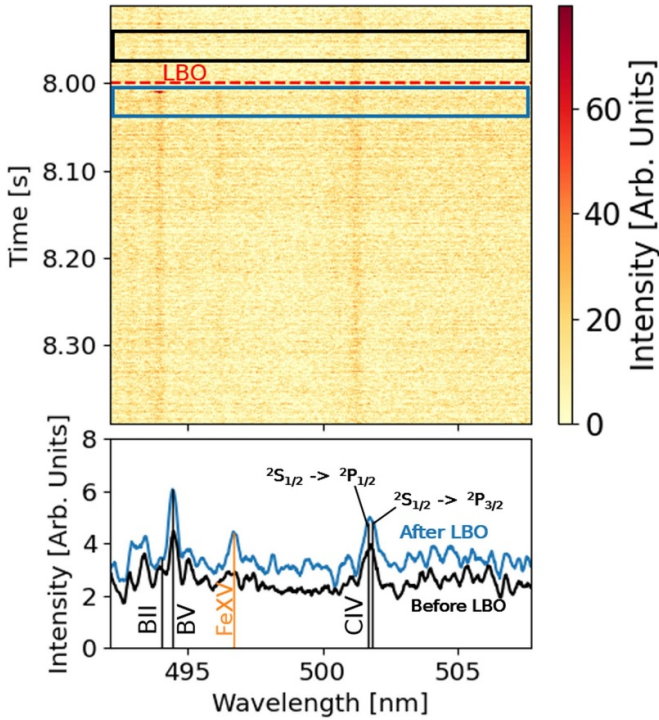
Figure 8. Recorded spectrum following Fe LBO injection into a plasma with no neutral beam injection. The top plot shows the signal intensity in the color scale. Passive emission prior-to (after) the Fe injection is time-averaged over the range specified by the black (blue) box and plotted in the bottom window. (Program #20230314.41).
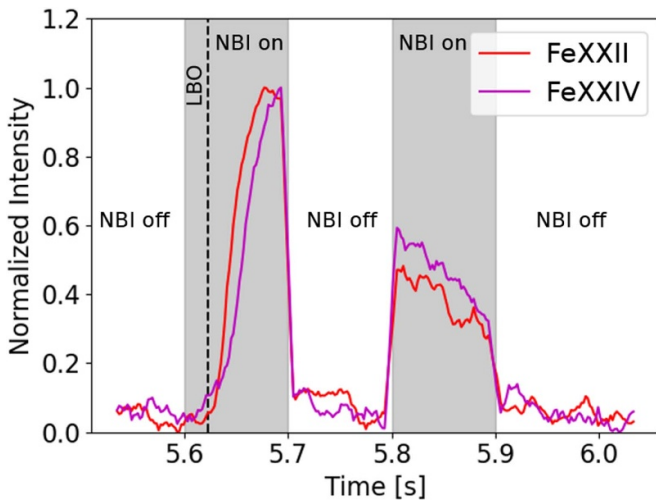

Figure 9. Recorded line intensities for Fe XXII and Fe XXIV following laser blow-off (LBO) injection into a plasma with the beam switched on and off with a frequency of 10 Hz and a duty cycle of 50% (Program # 20221201.38). Radiation from these high charge states exhibits little to no passive component. The signal collected in the NBI modulation phase before the LBO injection is given in faded colors.

the 'on' phases of the NBI. One can observe the rise in intensity of the various charge states during the first NBI period followed by an abrupt drop to zero during the period without NBI in the Fe XXII and XXIV signals. Once the beam is turned

back on, one can clearly see the Fe XXII and Fe XXIV signals return during which they are in their decay phase. This indicates that the measurement of Fe XXII and Fe XXIV radiation will provide excellent spatial resolution for use in impurity transport studies since the emission is localized along the neutral beam (i.e. there is essentially zero contribution from electron impact excitation).

From figure 9 one can also take note of the differing time characteristics of the signal coming from the two Fe charge states. It is clear that there is a slight delay in the signal rise time for Fe XXIV compared to Fe XXII. Such a discrepancy can be attributed mostly to the differing ionization rates. At a given temperature, the higher charge state will take longer to populate due to a reduced ionization rate (see figure 11 in [21]). Additionally, transport can affect the signal rise time as impurities can be driven to the core where the hotter temperatures can more quickly populate higher charge states. The highly ionized impurities can then diffuse outward before recombining. This mechanism then implies that careful observation of the signal rise times provides useful constraints on the impurity transport.

3.2. Impurity transport study on select experimental program

3.2.1. Experimental conditions. The capability of the new diagnostic and measurement technique based on high-n Rydberg transitions is demonstrated by analyzing program #20230314.26. An example of one collected spectrum is given in figure 5. In this experiment, the high mirror magnetic configuration [49] is used along with ~ 2.3 MW of electron cyclotron resonance heating (ECRH). 2 MW of continuous NBI is introduced for a period of 4 s during which iron is injected via LBO. Kinetic profiles for this plasma during the LBO injection are given in figure 10 along with the neoclassical radial electric field calculated via the DKES & neotransp code [50, 51]. The electron temperature and density are determined via Thomson scattering [52] whereas ion temperatures are determined via CXRS from C^{6+} ions [30, 53]. Additionally, the flux surface averaged background neutral density profile is shown which has been simulated using pyFIDASIM, as described in a previous publication [40]. It should be noted here that the absolute values of the neutral density remain uncertain but have only a small effect on the impurity dynamics. A sensitivity analysis including order of magnitude changes to the input neutral density profile is given in section 3.2.3. The experimental times have been shifted for the simulation such that the LBO injection occurs at $t = 0.005$ s. This allows for variation of the LBO timing by ± 2 ms which is characteristic of the uncertainty in the LBO time stamp (this analysis is given in section 3.2.3. Finally, CX signals were only seen on channels 2–8 therefore, only these seven signals are utilized for the Bayesian inference.

Note that the CXRS signals provide constraints on the impurity emission profile however, only emission from high charge states inside $r/a \sim 0.6$ is observed. Additionally, the signal-to-noise ratio of the measurements are not sufficient
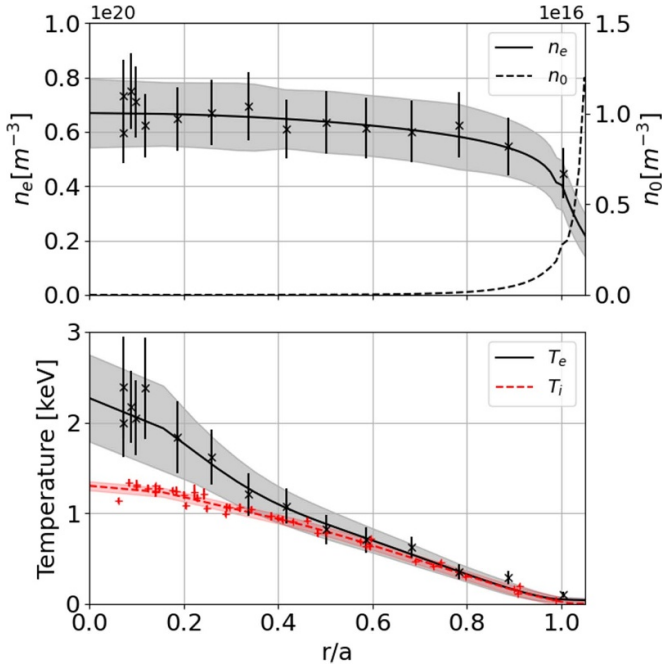
Figure 10. (*a*) Electron density profile measured by Thomson Scattering and neutral density profile calculated by pyFIDASIM. (*b*) Electron temperature profile measured by Thomson Scattering and ion temperature profile measured by CXRS. In each case, 68% confidence intervals are shown in the shaded regions. Data points used in the profile fitting are shown with markers and corresponding error bars.

to track the impurity decay rate after the ionization state distribution has reached an equilibrium (i.e. all of the charge states eventually decay away at the same rate). To provide additional constraints on the transport near the edge and the global decay time, two x-ray lines measured by the HEXOS diagnostic are included in the inference framework. The lines at 6.64 nm and 9.39 nm have been identified to correspond to the $2p^6f4(^2F_{7/2}) -> 2p^63d(^2D_{5/2})$ and $2s2p^6(^2S_{1/2}) -> 2s^22p^5(^2P_{3/2})$ transitions for the Fe XVI and XVIII charge states respectively. Unfortunately, for the OP 2.1 campaign at W7-X, the HEXOS diagnostic was partially damaged and an absolute calibration of the diagnostic was not available. For this reason, we choose to fit the normalized intensity of the two x-ray lines with a model similar to that described in [21].

3.2.2. Bayesian inference of impurity transport. An inference of the impurity diffusion and convection profiles is obtained by using the emcee package [54] which utilizes the Markov-Chain Monte Carlo (MCMC) method. For this analysis, Gaussian likelihoods are chosen for comparison of forward modeled and measured signals. The combination of the CXRS lines of sight and the HEXOS measurements is done by the so-called independent likelihood pool method [55].

Both the diffusion profile and the peaking ratio, rV/D, are parameterized by piece-wise cubic-Hermite interpolating polynomials (PCHIP) that enforce monotonicity in D or rV/D

between knot points. In this context, r refers to the effective minor radius of the LCFS. These profiles have three independent knot points that are allowed to vary in location such that they adhere to a minimum set distance. Additionally, in the scrape-off layer, the convection is set to zero and an ad-hoc diffusion of 0.5 m^2 s^{-1} is chosen.

To avoid user-defined biases, we choose fairly weak priors that only rule out nonphysical results. Here we take a similar approach to that described in previous studies at Alcator C-Mod [24]. First, since the diffusion could conceivably take on magnitudes characteristic of anything from classical to Bohm diffusion, the so-called 'Jefferys' prior is utilized which uniformly samples over $\log(D)$ within the bounds of 0.01 m^2 s^{-1} and 100 m^2 s^{-1}. The prior distribution for the peaking ratio, rV/D, is chosen to be a Gaussian centered around zero with a width of 10. This allows for both positive and negative peaking while ruling out nonphysical extremely peaked or hollow impurity density profiles. The six independent knot points (three for both D and rV/D) are allowed to vary with uniform priors such that the first knot point lies within $0 < r/a < 0.5$, the second within $0 < r/a < 1$ and the third within $0.5 < r/a < 1$. Additionally, it is enforced that the three knot points must be increasing in value and a minimum distance is enforced such that the prior probability gets exponentially smaller inside a distance of $\Delta r/a \sim 0.05$. For the 'effective' beam attenuation, a uniform prior is considered for the parameter $X_{\rm eff}$ between 0 and 1. Here $X_{\rm eff} = 0$ and $X_{\rm eff} = 1$ correspond to the cases where the effective beam attenuation sits up against the lower or upper bound of the grey-shaded region depicted in figure 4. Values between 0 and 1 correspond to a linear interpolation between the two extremes. Finally, a prior for the loss rate in the edge ($\omega_\parallel$ in equation (1)) is described again by the Jefferys prior while being allowed to vary from 3×10^2 s^{-1} to 3×10^3 s^{-1}. This spans an order of magnitude centered at an estimate for the loss rate based on a divertor connection length of 10 m and impurities streaming along field lines at thermal velocities.

The matched signals for the CXRS measurements and the HEXOS diagnostic are given in figures 11 and 12 respectively. Moreover, the corresponding inferred impurity diffusion and convection profiles are given in figure 13. For most channels, we achieve good agreement for not only the decay, but also the impurity rise times and the relative intensities. For line of sight 3, the temporal behavior is not reproduced perfectly for the Fe XXII emission. One potential explanation is that this effect is not captured by the model due to the assumption of time-independent kinetic profiles. Core and mid-radius electron cyclotron emission (ECE) measurements indicate that there is a brief period of $\sim$40% reduction in the electron temperature before the profile recovers $\sim$10ms later. During this period, temperatures at the locations of the active emissions seen by the inner lines of sight may still be sufficiently high that ionization up to the Fe^{22+} charge state is fast. Line of sight 3 however, views local emission from a location in the plasma where the electron temperature is $\sim$800 eV. This temperature range is close to the left edge seen in figure 7 associated with a sharp drop-off in the ionization

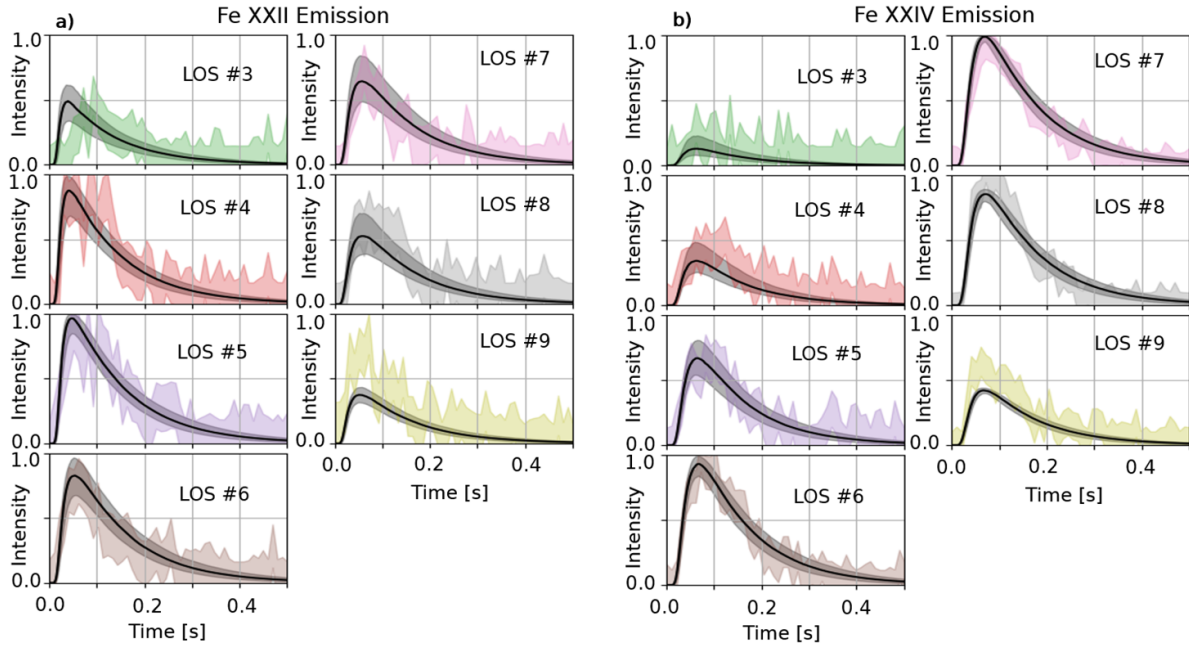**Figure 11.** Fitted CXRS signals for the Fe XXII line emission (*a*) and Fe XXIV line emission (*b*) shown in black with the fitting uncertainty shaded in grey. Statistical uncertainty is shown with color coding corresponding to that done in figure 2. Each signal is normalized such that the brightest channel has a peak intensity of 1. For the case of the Fe XXII and Fe XXIV emission, an intensity of 1 corresponds to a Radiance of 2.9×10^{15} photons $m^{-2} sr^{-1} s^{-1}$ and 3.8×10^{15} photons $m^{-2} sr^{-1} s^{-1}$ respectively.
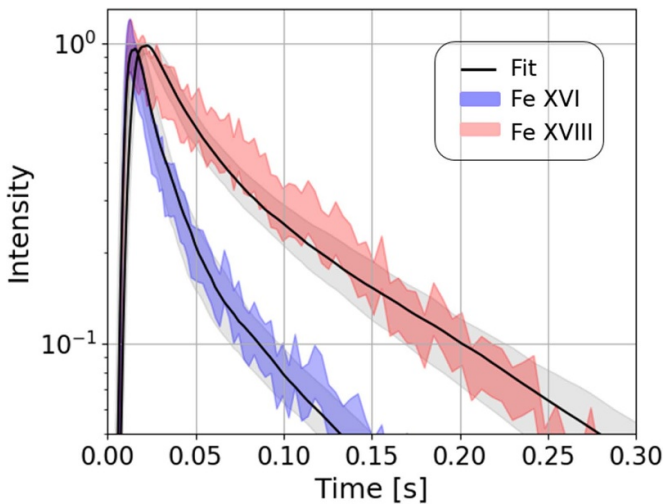

Figure 12. Fitted HEXOS Fe XVI and Fe XVIII line emission at 6.64 nm and 9.39 nm respectively shown in black with fitting uncertainty (68% confidence) in shaded grey. Error bands for the measured signals are given in blue and red.

rate. Additionally, there is some disagreement in the fitted intensity for line of sight 9 which is likely due to the simplified beam attenuation model. Nevertheless, the overall good agreement between synthetic and measured diagnostics indicates that the inferred diffusion and convection profiles (given in figure 13) can explain the observed impurity emissivities. In this experiment, the impurity CX signals can be explained

by a large anomalous diffusion exceeding the expected contribution from neoclassical transport. Error bars here are calculated by re-sampling from the posterior distribution, generating diffusion and convection profiles for each sample, and calculating statistical uncertainties at each point in r/a. This result is consistent with expectation since ion temperature gradient turbulence likely dominates the diffusion outside of the mid-radius [56]. Additionally, both the diffusion profile shape and magnitude are compatible with previous studies of impurity transport on W7-X based on the HEXOS diagnostic [21, 22]. Inferred convection velocities are negative within the mid-radius and large compared to neoclassical predictions. This result is consistent with nonlinear gyrokinetic simulations performed for $r/a \sim 0.5$ (albeit in the standard magnetic configuration) [9] which have predicted negative pinch contributions in ion temperature gradient dominated turbulence scenarios.

3.2.3. Sensitivity study. To illustrate the effect of the uncertainty in a variety of model inputs, several additional inferences were carried out. Here, we consider variations in the electron temperature (T_e) and density (n_e), the ion temperature (T_i), the LBO injection timing (t_{LBO}), the edge neutral density (n_0) magnitude, and the ad-hoc edge diffusion value (D_{edge}). Electron temperature and density profiles as well as ion temperatures are varied between the upper and lower bounds of the error bars shown in figure 10. There are large uncertainties in the edge neutral density and therefore the profile used in the
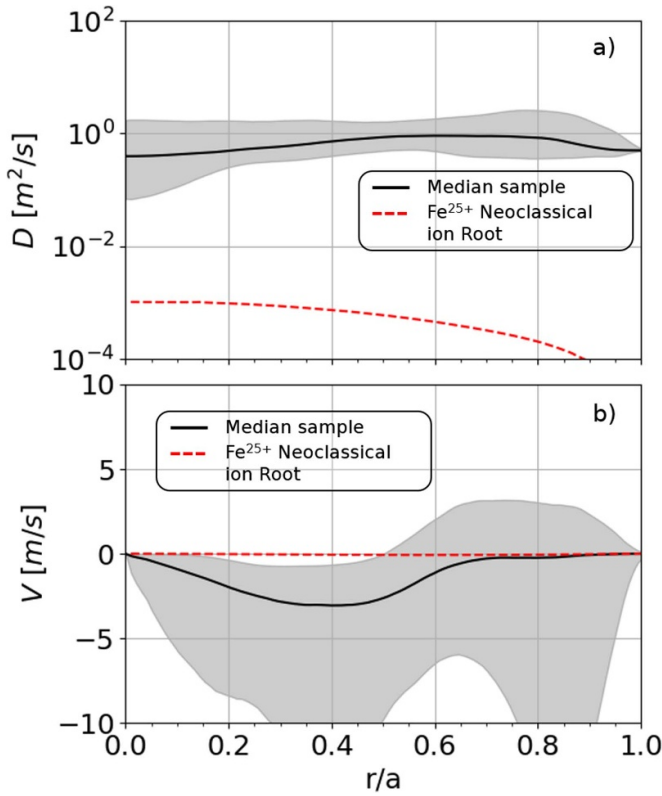
Figure 13. Fitted (*a*) diffusion and (*b*) convection profiles which describe the measured CXRS and HEXOS signals. Shaded regions correspond to the 1 sigma error bands based on a subset of D and V profiles resampled from the posterior distribution. Neoclassical transport coefficients calculated by neotransp are shown via the dashed lines.

Figure 14. Median (*a*) diffusion and (*b*) peaking ratio profiles for varied inputs to the Bayesian inference model with color coding depicting which parameter is varied. Positive changes to the parameter of interest are given in dashed lines while negative changes are given in dot-dashed lines. The base case considered in the previous section is shown in solid black with fitting uncertainty shown in shaded grey.

previous section is scaled by a factor of between 0.1 and 10. To account for the uncertainty in the LBO timing of ∼ms the pySTRAHL LBO source function is shifted in time by ± 2 ms. Finally, the ad-hoc edge diffusion is varied by ± 50 %. The median sample impurity diffusion and peaking ratios for each case are shown in figure 14. In nearly every case, similar transport profiles are inferred. The most notable effect is perhaps in the variation of the electron temperature profile where an elevated temperature requires lower diffusion near the edge to reproduce the signals while reduced temperatures require heightened diffusion. This can be explained by the requirement that impurities must be transported into regions where they can ionize quickly. For increased or reduced temperatures, this ionization region would be shifted towards the edge or core respectively. Additionally, the case of reduced temperature exhibits reduced sensitivity to the core peaking ratio with the median sample indicating a negligible pinch contribution. It can also be noted that the ad-hoc SOL diffusion has a strong effect on the magnitude of the diffusion around $r/a = 0.8$. As one might expect, a smaller SOL diffusion is compensated by a large diffusion near the edge to bring impurities into the core more quickly with the opposite effect observed for heightened
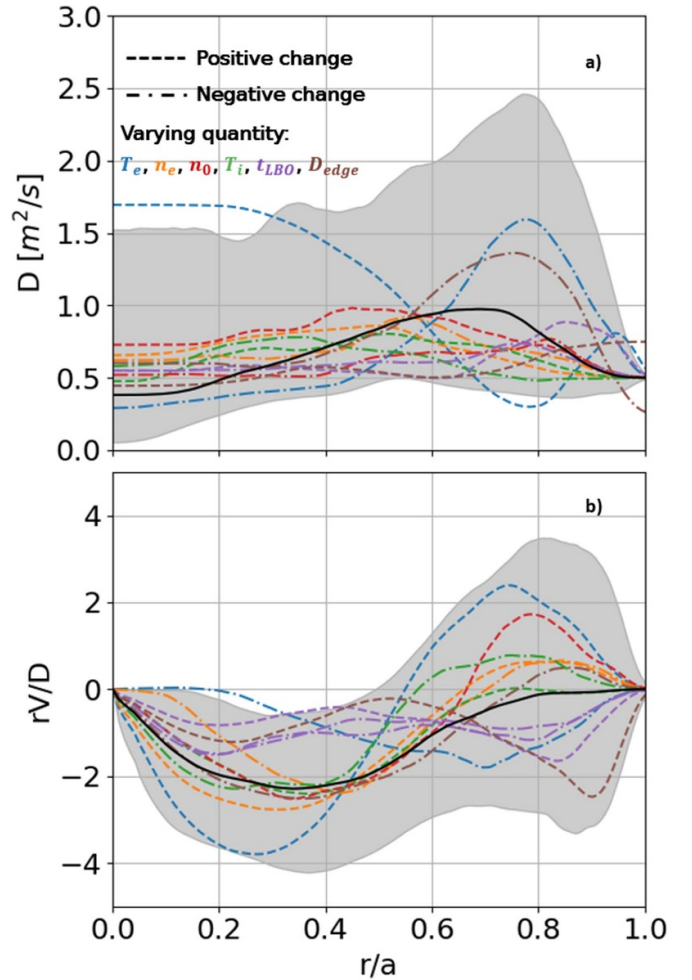
SOL diffusion. Finally, all but the increased electron temperature solutions would fall within the error bars given for the base fit result shown in figure 11.

4. Discussion

In this paper, the observation of high-n Rydberg emissions from Fe injections were used to infer impurity transport characteristics in W7-X with enough certainty to indicate an impurity pinch velocity in the core. It should be noted that the absence of passive emission is a benefit which is characteristic of highly ionized impurities. For future studies, one should consider the expected ionization balance based on the plasma background and compare with typical background neutral profiles. Such predictions can be done either through

a coronal equilibrium calculation similar to that shown in figure 7 or via a collisional radiative transport model such as STRAHL/pySTRAHL. Passive signals could be modeled as well though careful accounting for the 3D distribution of background neutrals would be necessary.

In terms of the transport analysis, the value of reliable uncertainty estimates should not be understated. Specifically at W7-X, reliable quantification of measurement error for inferred transport has not been reported [21, 22]. While the wide uncertainty in the inferred transport parameters may at first seem underwhelming, it is important to note that their accounting allows for one to make statements on the nature of the transport with increased confidence. Future efforts may necessitate comparison to impurity transport calculations performed with gyrokinetic simulations such as GENE and in such cases, narrower uncertainties may be required. Since the study presented here is a first attempt at using Rydberg-like emissions to constrain impurity transport, improvements can be made to the framework to provide stronger constraints on the inferred values.

5. Conclusion and outlook

In this paper, we have shown that the newly installed, intensity calibrated, fast CXRS system at W7-X is able to measure localized impurity radiation with temporal resolutions sufficient to fit the rise and decay times as well as the relative intensities following LBO injection. This enables, for the first time at W7-X, simultaneous inference of both the impurity diffusion and convection profiles. By observing high-n Rydberg transitions, we can image line radiation from a variety of charge states of any highly ionized heavy impurity without a significant passive spectral component. Additionally, synthetic diagnostics can be calculated by considering the sight lines of the spectrometers and simulating the transport of impurities with the code pySTRAHL. Finally, impurity diffusion and convection profile reconstructions are possible and have been performed for one LBO experiment which took place during the OP 2.1 campaign. In the analyzed discharge, observed impurity emissions can be explained by an anomalous diffusion profile consistent with previous studies [21, 22] and a convection velocity qualitatively consistent with simulation.

As follow-up work, several improvements can be made to the analysis. For example, several mechanisms which are known to affect impurity transport are neglected here such as the possibility of charge state dependence on the transport coefficients and the potential for poloidal asymmetries in the impurity densities [57]. Future modeling work could attempt to capture these considerations. Additionally, inference uncertainties may be reduced by including additional measurements from a variety of relevant diagnostics in the modeling framework. Diagnostics such as crystal x-ray spectroscopy (HRXIS) [58], core bolometry [59], soft x-ray multi-camera tomography (XMCTS) [60], and Z_{eff} measurements [61] may prove useful in this regard. Specifically, the HRXIS and XMCTS measurements can provide additional constraints on the impurity transport while the bolometer and Z_{eff} measurements can be used to determine the total number of injected particles.

ORCID iDs

Colin Swee ⓘ https://orcid.org/0000-0003-2365-6777
Benedikt Geiger ⓘ https://orcid.org/0000-0001-8706-1874
Mark Nornberg ⓘ https://orcid.org/0000-0003-1786-4190
Martin O'Mullane ⓘ https://orcid.org/0000-0002-2160-4546
Peter Poloskei ⓘ https://orcid.org/0000-0001-7781-5599
Thilo Romba ⓘ https://orcid.org/0000-0002-2727-9385
Thomas Wegner ⓘ https://orcid.org/0000-0003-0136-0406

References

[1] Angioni C. 2021 *Plasma Phys. Control. Fusion* **63** 073001
[2] Buller S., Smith H.M. and Mollén A. 2021 *Plasma Phys. Control. Fusion* **63** 054003
[3] Nozato H., Morita S., Goto M., Takase Y., Ejiri A., Amano T., Tanaka K. and Inagaki S. (LHD Experimental Group) 2004 *Phys. Plasmas* **11** 1920–30
[4] Nozato H., Morita S., Goto M., Takase Y., Ejiri A., Amano T., Tanaka K. and Inagaki S. (LHD Experimental Group) 2006 *Phys. Plasmas* **13** 092502
[5] Huang X., Morita S., Oishi T., Murakami I., Goto M., Zhang H. and Liu Y. (The LHD Experiment Group) 2017 *Nucl. Fusion* **57** 086031
[6] Burhenn R. *et al* 2004 *Fusion Sci. Technol.* **46** 115–28
[7] Zurro B. *et al* 2003 Transport analysis of impurity injected by laser ablation in the TJ-II stellarator *30th European Physical Society Conf. on Plasma Physics and Controlled Fusion* (*St. Petersburg, Russian Federation*) (available at: https://citeseerx.ist.psu.edu/document?repid=rep1&type=pdf&doi=fef5456b8b523356cb55a074aecd8c5bd2229c73) (European Physical Society)
[8] Helander P. *et al* 2012 *Plasma Phys. Control. Fusion* **54** 124009
[9] García-Regaña J.M. *et al* 2021 *J. Plasma Phys.* **87** 855870103
[10] García-Regaña J., Barnes M., Calvo I., González-Jerez A., Thienpondt H., Sánchez E., Parra F.I. and St.-Onge D.A. 2021 *Nucl. Fusion* **61** 116019
[11] Marmar E.S., Cecchi J.L. and Cohen S.A. 1975 *Rev. Sci. Instrum.* **46** 1149–54
[12] Cohen S.A., Cecchi J.L. and Marmar E.S. 1975 *Phys. Rev. Lett.* **35** 1507
[13] Isler R. 1984 *Nucl. Fusion* **24** 1599
[14] Pasini D. *et al* 1990 *Nucl. Fusion* **30** 2049

[15] Burhenn R. and Weller A. (W7-AS Team, NI Group and The ECRH Group) 1999 *Rev. Sci. Instrum.* **70** 603–7

[16] Scavino E., Bakos J.S., Dux R. and Weisen H. (TCV Team) 2003 *Plasma Phys. Control. Fusion* **45** 1961

[17] Burhenn R. *et al* 2009 *Nucl. Fusion* **49** 065005

[18] Howard N.T., Greenwald M. and Rice J.E. 2011 *Rev. Sci. Instrum.* **82** 033512

[19] Zurro B. *et al* 2011 *Nucl. Fusion* **51** 063015

[20] Wegner T. *et al* 2018 *Rev. Sci. Instrum.* **89** 073505

[21] Geiger B. *et al* 2019 *Nucl. Fusion* **59** 046009

[22] Wegner T. *et al* (W7-X Team) 2020 *Nucl. Fusion* **60** 124004

[23] Odstrčil T. *et al* 2020 *Phys. Plasmas* **27** 082503

[24] Sciortino F. *et al* 2020 *Nucl. Fusion* **60** 126014

[25] Reinke M.L., Beiersdorfer P., Howard N.T., Magee E.W., Podpaly Y., Rice J.E. and Terry J.L. 2010 *Rev. Sci. Instrum.* **81** 10D736

[26] Cheng Y. *et al* 2022 *Rev. Sci. Instrum.* **93** 123501

[27] Oishi T., Morita S., Dai S.Y., Kobayashi M., Kawamura G., Huang X.L., Zhang H.M., Liu Y. and Goto M. 2017 *Nucl. Fusion* **58** 016040

[28] Olson R.E. 1981 *Phys. Rev.* A **24** 1726–33

[29] Fonck R.J., Darrow D.S. and Jaehnig K.P. 1984 *Phys. Rev.* A **29** 3288–309

[30] Ford O.P. *et al* (W7-X Team) 2020 *Rev. Sci. Instrum.* **91** 023507

[31] Romba T., Reimold F., Jaspers R., Ford O., Vanó L. and Klinger T. 2023 *Nucl. Fusion* **63** 076023

[32] McDermott R.M. *et al* 2018 *Plasma Phys. Control. Fusion* **60** 095007

[33] Kumar S.T.A., Hartog D.J.D., Chapman B.E., O'Mullane M., Nornberg M., Craig D., Eilerman S., Fiksel G., Parke E. and Reusch J. 2011 *Plasma Phys. Control. Fusion* **54** 012002

[34] Kappatou A., Jaspers R.J.E., Delabie E., Marchuk O., Biel W. and Jakobs M.A. 2012 *Rev. Sci. Instrum.* **83** 10D519

[35] Li Y.Y. *et al* 2014 *Rev. Sci. Instrum.* **85** 11E428

[36] Stratton B.C. *et al* 1991 *Nucl. Fusion* **31** 171–5

[37] Sciortino F. *et al* 2022 *Plasma Phys. Control. Fusion* **64** 124002

[38] Geiger B. *et al* 2020 *Plasma Phys. Control. Fusion* **62** 105008

[39] Swee C., Geiger B., Albosta R., Ford O., Loch S., Nornberg M.D., Schellpheffer J. and Wegner T. 2022 *Rev. Sci. Instrum.* **93** 103523

[40] Swee C., Geiger B., Dux R., Kumar S.T.A., Castillo J.F., Bader A. and Gerard M. 2022 *Plasma Phys. Control. Fusion* **64** 015008

[41] Janev R.K., Boley C.D. and Post D.E. 1989 *Nucl. Fusion* **29** 006

[42] McDermott R., Dux R., Guzman F., Pütterich T., Fischer R. and Kappatou A. (The ASDEX Upgrade Team) 2020 *Nucl. Fusion* **61** 016019

[43] Bussiahn R., Tamura N., McCarthy K.J., Burhenn R., Hayashi H., Laube R. and Klinger T. (LHD Experiment Group and W7-X Team) 2018 *Rev. Sci. Instrum.* **89** 10K112

[44] Suto K. 2020 *J. Mod. Phys.* **11** 712–24

[45] Haug E.G. 2020 *J. Mod. Phys.* **11** 105731

[46] Thorman A. *et al* 2021 *Phys. Scr.* **96** 125631

[47] Arnaud M. and Raymond J. 1992 *Astrophys. J.* **398** 394

[48] Summers H. 2004 The ADAS user manual, version 2.6 (available at: www.adas.ac.uk)

[49] Dinklage and A. *et al* 2018 *Nat. Phys.* **14** 855–60

[50] Spong D.A. 2005 *Phys. Plasmas* **12** 056114

[51] Smith H. 2020 Neotransp *Technical Report* (IPP Greifswald) (available at: https://gitlab.mpcdf.mpg.de/smithh/neotransp)

[52] Pasch E., Beurskens M.N.A., Bozhenkov S.A., Fuchert G., Knauer J. and Wolf R.C. (W7-X Team) 2016 *Rev. Sci. Instrum.* **87** 11E729

[53] Jaspers R.J.E. *et al* 2012 *Rev. Sci. Instrum.* **83** 10D515

[54] Foreman-Mackey D., Hogg D.W., Lang D. and Goodman J. 2013 *Publ. Astron. Soc. Pac.* **125** 306–12

[55] Von Toussaint U. 2011 *Rev. Mod. Phys.* **83** 943–99

[56] Proll J.H.E., Xanthopoulos P. and Helander P. 2013 *Phys. Plasmas* **20** 122506

[57] Zhang D. *et al* 2021 *Nucl. Fusion* **61** 116043

[58] Langenberg A. *et al* 2018 *Rev. Sci. Instrum.* **89** 10G101

[59] Zhang D. *et al* 2010 *Rev. Sci. Instrum.* **81** 10E134

[60] Brandt C. *et al* 2020 *Plasma Phys. Control. Fusion* **62** 035010

[61] Pavone A. *et al* 2020 *J. Instrum.* **15** e02002